Why Multilayer Graphene on 4H-SiC$(000\bar{1})$ Behaves Like a Single Sheet of Graphene

J. Hass,[1] F. Varchon,[2] J. E. Millán-Otoya,[1] M. Sprinkle,[1] N. Sharma,[1] W. A. de Heer,[1] C. Berger,[1,2] P. N. First,[1] L. Magaud,[2] and E. H. Conrad[1]

[1]*The Georgia Institute of Technology, Atlanta, Georgia 30332-0430, USA*
[2]*Institut Néel/CNRS-UJF BP166, 38042 Grenoble Cedex 9, France*

(Received 13 June 2007; published 28 March 2008)

We show experimentally that multilayer graphene grown on the carbon terminated SiC$(000\bar{1})$ surface contains rotational stacking faults related to the epitaxial condition at the graphene-SiC interface. Via first-principles calculation, we demonstrate that such faults produce an electronic structure indistinguishable from an isolated single graphene sheet in the vicinity of the Dirac point. This explains prior experimental results that showed single-layer electronic properties, even for epitaxial graphene films tens of layers thick.

DOI: 10.1103/PhysRevLett.100.125504 PACS numbers: 68.35.−p, 61.05.cp, 61.05.jh, 68.55.−a

An intriguing series of experiments suggests that a new all-graphene based paradigm for electronic circuits may be possible [1–6]. In this system, graphene sheets are lithographically cut into ribbons to control the electronic structure [7–9], and to produce gates and wires from a single material [1]. To become a viable technology, wafer-scale graphene must be grown on a substrate while preserving the electronic properties of an isolated graphene sheet. A potential platform is epitaxial graphene on SiC(0001) [1] or SiC$(000\bar{1})$ [5]. Multilayer graphene films furnace-grown on SiC$(000\bar{1})$ (C-face), typically 10–20 graphene layers thick, exhibit high carrier mobilities with characteristics of highly doped ($\sim 4 \times 10^{12}$ cm^{-2}) single-layer graphene (Berry phase of π, antilocalization) [5,10]. Infrared transmission measurements [11,12] are also consistent with undoped single-layer graphene. The paradox is that graphitic AB stacking breaks the equivalency of sublattice atoms in a graphene sheet [13,14] so that multilayer films should not exhibit the graphenelike properties that are clearly observed. While a buffer layer near the SiC interface and its related charge transfer [15,16] could produce a doped, high-mobility layer, the overlying graphene multilayer—beyond a screening length of 1–2 layers—would remain neutral [17]. Therefore, the source of *single-layer electronic properties* in the transport region and especially in the undoped multilayer must be identified.

In this Letter, we show that nature provides a new stacking sequence in C-face grown films that preserves the electronic symmetry of an isolated graphene sheet. Unlike Si-face films, C-face epitaxial graphene can grow in multiple forms: layers rotated 30° ($R30$), or ±2.20° ($R2^{\pm}$) from the SiC bulk $[10\bar{1}0]$ direction. In contrast, Si-face films orient only in the $R30$ phase (known as the $6\sqrt{3} \times 6\sqrt{3}R30°$ reconstruction in SiC coordinates) [18]. Surface x-ray diffraction (SXRD) and scanning tunnelling microscopy (STM) data on C-face films confirm that all three rotated phases are interleaved in the film, causing a high density of stacking fault boundaries between the $R30$ and $R2^{\pm}$ layers. *Ab initio* electronic calculations for this faulted stacking show that adjacent rotated planes become electronically decoupled, preserving the Dirac dispersion at the K-point, and thus maintain the electronic properties of an isolated graphene sheet.

All substrates were 4H-SiC$(000\bar{1})$ prepared as reported previously [19]. The SXRD experiments were performed at the Advanced Photon Source on the 6IDB- and C-μCAT beam lines at 16.2 keV photon energy. Reciprocal space points are reported in the reciprocal lattice units (r.l.u.) of the standard graphite hexagonal reciprocal lattice, $\mathbf{q} = (h\mathbf{a}^*, k\mathbf{b}^*, \ell\mathbf{c}^*)$, where $|\mathbf{a}^*| = |\mathbf{b}^*| = 2\pi/(a\sqrt{3}/2)$ and $|\mathbf{c}^*| = (2\pi/c)$. The nominal lattice constants for graphite are $a = 2.4589$ Å, $c = 6.708$ Å [20].

While it is known that graphene grows epitaxially only in the $R30$ phase on the SiC(0001) Si-face, multilayer graphene grown on the C-face was thought to have a high degree of azimuthal disorder because of streaking in low energy electron diffraction (LEED) images [18]. However, a detailed look at the diffraction shows that the source of these streaks is not random rotational disorder. This is demonstrated in the LEED image of Fig. 1(a), from a film with ~10 graphene layers. The pattern shows: (i) an oriented $R30$ film evidenced by graphene spots rotated ±30° from the SiC $[10\bar{1}0]$ direction and (ii) azimuthally diffuse split arcs centered at 0° from the SiC $[10\bar{1}0]$ direction. The splitting is seen more clearly in Fig. 1(b) where a SXRD azimuthal scan (ϕ scan) around $\phi = 0°$ is taken at the radial position of a graphite rod. The scan shows intensity peaked at $\phi = \pm 2.2°$ with widths of ~2.7°.

The significance of the ±2.2° preferred rotation is twofold. First, graphene is commensurate with the SiC substrate when a 13×13 graphene unit cell is rotated 30° from SiC. The 13×13 cell is ~0.14% smaller than a SiC $6\sqrt{3} \times 6\sqrt{3}$ $R30°$ cell. What has not been recognized is that there are two other ways to orient a 13×13 graphene sheet that have the same commensurability with the SiC $6\sqrt{3} \times 6\sqrt{3}$ $R30°$ structure. They occur when

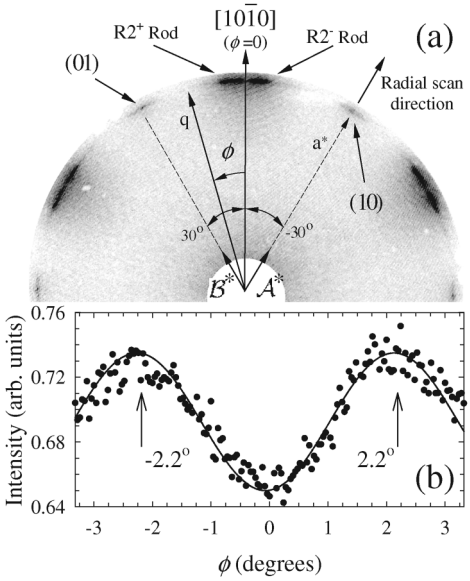

FIG. 1. (a) LEED image acquired at 67.9 eV from 4H-SiC(000$\bar{1}$) with ~10 graphene layers, showing only graphene spots and diffuse arcs. Shown for reference are the SiC [10$\bar{1}$0] direction and the SiC $6\sqrt{3}\times 6\sqrt{3}R30°$ reciprocal lattice vectors $\mathcal{A}^*$ and $\mathcal{B}^*$. (b) X-ray azimuthal scans of the diffuse graphite arc around $\phi = 0$ and $|q| = |a^*|$.

$$|n\mathcal{A}^* + m\mathcal{B}^*| \approx |\mathbf{a}^*|, \tag{1}$$

with n and m integers. $\mathcal{A}^*$ and $\mathcal{B}^*$ are the reciprocal lattice vectors of the $(6\sqrt{3}\times 6\sqrt{3})R30°$ structure [see Fig. 1(a)], $|\mathcal{A}^*| = |\mathcal{B}^*| = |a^*_{\mathrm{SiC}}|/(6\sqrt{3})$ with $a^*_{\mathrm{SiC}} = 2.3554$ Å^{-1}. The rotation angle of the graphene relative to SiC can be calculated for different m and n's satisfying Eq. (1):

$$\cos\phi = (\sqrt{3}/2)(n+m)(n^2+m^2+nm)^{-1/2}. \tag{2}$$

Equation (1) is satisfied when $(n, m) = (13, 0)$, (8,7), or (7,8). All three solutions give the SiC $6\sqrt{3}\times 6\sqrt{3}$ $R30°$ cell; the first with graphene rotated 30° relative to SiC while the other two give graphene rotated $\pm 2.204°$ relative to SiC. As Fig. 1(a) clearly shows, all three rotated phases can appear in C-face grown multilayer graphene. The two spots near $\phi = 0$ are indexed as the (8/13, 7/13, ℓ) and (7/13, 8/13, ℓ) graphene rods. For simplicity, we will refer to them as the $R2^{\pm}$ rods.

The significance of these three phases is even greater if we recognize that two stacked graphene sheets can be rotated relative to each other in a number of ways that make the two sheets commensurate [21]. The lowest energy commensurate rotation angles are precisely $\phi = \cos^{-1}(11/13)$ or $\cos^{-1}(23/26)$, i.e., $30 \pm 2.204°$ [21]. This bi-layer structure corresponds to a graphene $\sqrt{13}\times\sqrt{13}(R \pm 46.1°)$ cell. A schematic of such a fault pair is shown in Fig. 2(a).

While the observation of three rotational phases is interesting, it is their stacking that bears directly on the film's electronic properties. We now show that $R30$ and $R2^{\pm}$ graphene sheets are interleaved to produce a high density

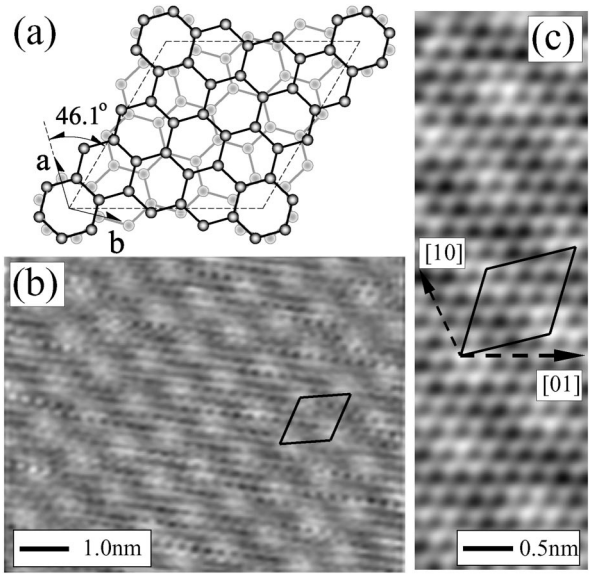

FIG. 2. (a) Schematic $\sqrt{13}\times\sqrt{13}R46.1°$ fault pair unit cell (dashed line). Dark circles are $R30$ C atoms (**a** and **b** are graphene unit vectors). Gray circles are C atoms in the $R2^+$ plane below, rotated 32.204° from the top plane. (b) STM image of C-face graphene showing a periodic superlattice with a $\sqrt{13}\times\sqrt{13}$ cell. (c) High resolution STM image (100 pA constant current, −0.8 V sample bias) of the $\sqrt{13}\times\sqrt{13}R46.1°$ unit cell (solid line) and the principle graphene directions (dashed lines). For display, Gaussian smoothing was used in (c) to reduce the atomic corrugation (15–20 pm peak-to-peak in the raw data) relative to the superlattice (~8 pm peak-to-peak).

of $R30/R2^{\pm}$ fault pairs instead of occurring as AB stacked $R30$ or $R2^{\pm}$ isolated domains. The most direct evidence for this is a surface reconstruction measured by STM [see Figs. 2(b) and 2(c)]. The images show a $\sqrt{13}\times\sqrt{13}$ unit cell rotated 46.1° from the graphene lattice with the lattice constant $a_{\sqrt{13}} = 8.9$ Å shown in Fig. 2(a). The existence of this structure means that at least one rotational fault pair exists near the graphene surface. SXRD further shows that these faults are not just near the surface but occur throughout the film. Figure 3(a) shows x-ray radial scans through the graphite (1, 0, ℓ) rod ($R30$ rod) for different values of $q_z = 2\pi\ell/c$. The two peaks correspond to a normal graphene (1, 0, ℓ) surface rod and the other to a graphene surface rod (1 + Δh, 0, ℓ) with a compressed in-plane lattice constant ($R30$ compressed rod). The peak separation corresponds to an in-plane compression of $\Delta a/a = -0.28 \pm 0.01\%$. We emphasize that the strain is not due the graphene-SiC lattice mismatch, which would *increase* the in-plane lattice constant. Note also that the compressed and uncompressed $R30$ rod widths are the same, meaning that the ordered, atomically flat domain size of both types of graphene sheets are similar (>3000 Å). This domain size is a lower limit on the size of continuous graphene sheets because graphene grows over the SiC steps [22], destroying the effective x-ray coherence (estimates from Raman, STM, and transport measurements indicate that

graphene domains are much larger, 4000–10 000 Å [5,23]). This clearly demonstrates that the compressed graphene is not due to lateral domain boundaries. Evidence that the compressed graphene occurs at the rotational stacking fault boundaries is presented below. Note that the $R2^{\pm}$ rod widths [see Fig. 3(b)] are the same as the $R30$ rods, indicating large sheets of this phase as well.

To show that the $R2^{\pm}$ rotated and compressed graphene layers are interleaved in the $R30$ stack, we have investigated the graphene stacking with SXRD. If the different rotational phases existed as isolated domains, we would expect them to be AB stacked. Figure 3(c) shows integrated (radial and azimuthal) intensity modulation of the $R30$, $R30$ compressed, and $R2^{\pm}$ rods as a function of ℓ. The modulation period and amplitude are due to the stacking arrangement, which is clearly different for each rod. For comparison, the expected instrument corrected intensity for a 10-layer AB stacked film (solid line) is shown in Fig. 3(c). While the $R30$ rod has some characteristic of AB stacking, the $R30$ compressed and $R2^{+}$ rods do not. This data, in conjunction with the STM results, clearly show that the graphene grown on the C-face has rotated graphene sheets interleaved in a multilayer graphene film.

A better fit to the $R30$ rod intensity can be made using a model where random rotational faults are introduced into the AB stack with a probability γ. To describe all the data, we allow both an in-plane lattice contraction (the source of the compressed $R30$ rod) and an interplanar expansion of ϵ (with respect to the bulk spacing) at each fault pair boundary. The interplanar expansion is revealed in the inset of Fig. 3(c) where the experimental peak near $\ell = 2$ is seen to be shifted to a slightly lower value. This expansion ($1.8 \pm 0.3\%$) is similar to azimuthally disordered turbostratic graphite, where rotational faults cause significant interference of π^{*} states between rotated planes [20]. Note that C-face graphene is *not* turbostratic since its domain sizes are much larger than the best turbostratic graphite samples ($\lesssim$1000 Å) and are not randomly oriented [24]. Also note that the interplanar expansion coupled with the in-plane contraction at the fault is consistent with graphite's negative in-plane and positive out-of-plane thermal expansion [25]. A weaker bond caused by the interlayer expansion at the fault allows the in-plane bonds to contract [25,26].

A fit to the $R30$ rod intensity with $\gamma = 0.38 + 0.07/-0.03$ and $\epsilon = 0.06 \pm 0.02$ Å for a 10-layer film is shown in Fig. 3(c). This model fits the data better than simple AB stacking. We have also estimated γ from the relative intensities of all three rods at $\ell = 0$. This is because in a random model at $\ell = 0$, the diffraction intensity is proportional to the square of the probability of finding each type of rotated layer: $I_{R30}/I_{R30\text{comp}} = 4(1-\gamma)^4/\gamma^4$ and $I_{R30}/I_{R2^-} = (1-\gamma)^2/\gamma^2$. This method gives slightly higher fault densities, $\gamma = 0.5 \pm 0.06$. Measurements from samples with graphene films thicknesses of 8, 10, and 30 layers give consistent values of γ ranging from 0.45–0.6.

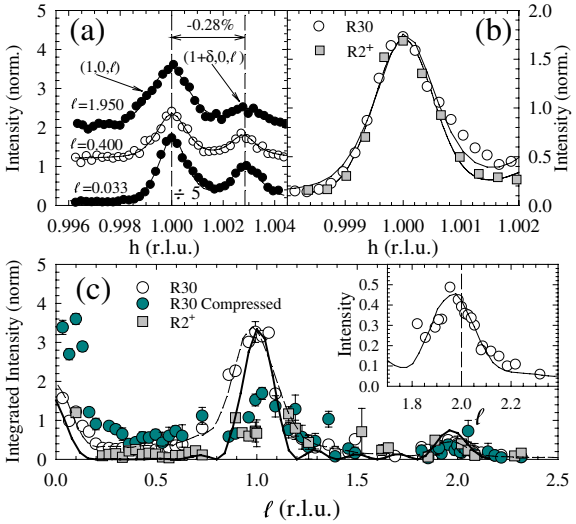

FIG. 3 (color online). (a) Radial (h) scans through the graphite ($h = 1, 0, \ell$) rod for different ℓ (see Fig. 1). Scans show two peaks corresponding to the normal graphene (1, 0, ℓ) rod and a compressed graphene ($1 + \Delta h$, 0, ℓ) rod. (b) Comparison of radial scans through the $R30$ and $R2^{+}$ rods at $\ell = 0.1$. (c) Integrated intensity of the $R30$, $R30$-compressed, and $R2^{+}$ rods. Solid line is a fit for 10 graphene layers AB stacked. Dashed line is a fit for 10 graphene layers with a random rotational fault model. Inset is an expanded view near $\ell = 2$.

We expect significant changes in the electronic properties of the graphene films when the rotational fault density is high. Because only 2 atoms/sheet out of 52 in the $\sqrt{13} \times \sqrt{13}R \pm 46.1°$ faulted cell are in high symmetry atom--over-atom positions, the interplanar interactions will be weaker at the fault. To understand how the observed stacking affects the electronic properties of these films, we have performed an *ab initio* density functional theory (DFT) calculation of the band structure of a $R30/R2^{\pm}$ freestanding graphene fault pair. Calculations were performed using the VASP [27] code and the generalized gradient approximation [28]. Ultra soft pseudopotentials [29] are used with a plane wave basis cutoff equal to 211 eV. All calculations were performed on the same bi-layer commensurate cell shown in Fig. 2(a). The vacuum width is 24 Å. The total energy of the rotated stacking cell is 1.6 meV/atom higher than an AB cell. This energy difference is slightly smaller than other estimates of this structure [21]. For bi-layers, the interlayer distance is fixed to 3.39 Å. We have varied this distance and found no qualitative change in the results. This check was performed since DFT is known to poorly describe van der Waals forces and gives theoretical graphene interlayer spacings significantly larger than experiment. However, the C-short ultrasoft pseudopotential used here has been extensively tested and shown to correctly describe the band structure of graphite [15,30]. Integration over the Brillouin zone is performed on a $30 \times 30 \times 1$ grid in the Monckhorst-Pack scheme to ensure convergence of the Kohn-Sham eigenvalues. Because of the faulted cell symmetry, the K-points of the graphene 1×1 cell are

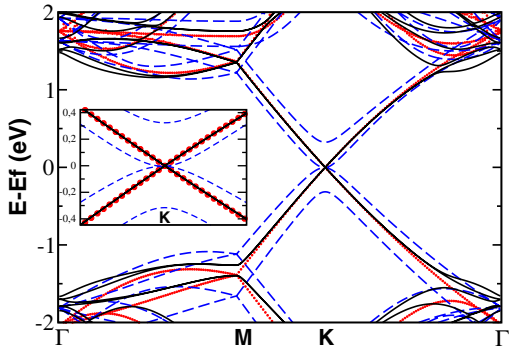

FIG. 4 (color online). Calculated band structure for three forms of graphene. (i) isolated graphene sheet (dots), (ii) $AB\ldots$ graphene bi-layer (dashed line), and (iii) $R30/R2^{+}$ fault pair (solid line). Inset shows details of band structure at the K-point.

translated to the K-point of the $\sqrt{13}\times\sqrt{13}R\pm 46.1°$ Brillouin zone.

The results of this calculation are shown in Fig. 4 where we compare the band structure for an isolated graphene sheet, a graphene bi-layer with AB stacking, and the bi-layer rotational fault pair of Fig. 2(a) [the $\Gamma-K-M$ directions are shown for the $\sqrt{13}\times\sqrt{13}R\pm 46.1°$ cell]. The main differences in the electronic structure of the three graphene forms appear in the dispersion curves near the K-points. The band structure for an isolated graphene sheet shows the known gapless linear dispersion (Dirac cone) of the π bands at the K-point. The AB stacked bi-layer lifts the sublattice symmetry, giving rise to splitting of the π bands and a change to parabolic bands [13,14]. With the rotational fault, the linear dispersion is recovered near the K-points and is identical to the graphene dispersion (same Fermi velocity). This implies that, in the rotated layers, atoms on the A and B sublattices are effectively identical. The linear dispersion at the K-point also holds for infinite stacks of rotational graphene fault pairs. This result is similar to the conclusions of Lopes dos Santos *et al.* [31], who considered much smaller rotations in a continuum model.

In conclusion, we show that multilayer graphene grown on the carbon terminated face of 4H-SiC does not grow as a simple AB stacked graphite film. Instead, graphene grows with a high density of rotational faults where adjacent sheets are rotated relative to each other. This is very different from HOPG graphite were rotational faults are only produced during sample cleaving [32]. Apparently, the graphene-SiC interaction, or growth kinetics, makes production of these faults more ubiquitous. We further show that these stacking faults decouple adjacent graphene sheets so that their band structure is nearly identical to isolated graphene. Specifically, the Dirac dispersion at the K-point is preserved even though the film is composed of many graphene sheets. This may explain why magneto-transport [5] and infrared magnetotransmission [11] experiments on C-face grown graphene give results very similar to those of an isolated graphene sheet.

We wish to acknowledge N. Wipf, G. Trambly de Laissardière, and D. Mayou for fruitful discussions about the energetics of rotated graphene. This research was supported by the NSF (Nos. ECCS-0404084, ECCS-0521041), by Intel Research, and CNRS. The Advanced Photon Source is supported by the DOE Office of Basic Energy Sciences, Contract No. W-31-109-Eng-38. The μ-CAT beam line is supported through Ames Lab, for the US DOE under Contract No. W-7405-Eng-82.

[1] C. Berger *et al.*, J. Phys. Chem. B **108**, 19912 (2004).
[2] K. S. Novoselov *et al.*, Science **306**, 666 (2004).
[3] Y. Zhang, Y.-W. Tan, H. L. Stormer, and P. Kim, Nature (London) **438**, 201 (2005).
[4] K. S. Novoselov *et al.*, Nature (London) **438**, 197 (2005).
[5] C. Berger *et al.*, Science **312**, 1191 (2006).
[6] A. K. Geim and K. S. Novoselov, Nat. Mater. **6**, 183 (2007).
[7] K. Nakada, M. Fujita, G. Dresselhaus, and M. S. Dresselhaus, Phys. Rev. B **54**, 17954 (1996).
[8] K. Wakabayashi, M. Fujita, H. Ajiki, and M. Sigrist, Phys. Rev. B **59**, 8271 (1999).
[9] M. Y. Han, B. Ozyilmaz, Y. Zhang, and P. Kim, Phys. Rev. Lett. **98**, 206805 (2007).
[10] X. Wu *et al.*, Phys. Rev. Lett. **98**, 136801 (2007).
[11] M. L. Sadowski *et al.*, Phys. Rev. Lett. **97**, 266405 (2006).
[12] M. L. Sadowski *et al.*, Solid State Commun. **143**, 123 (2007).
[13] B. Partoens and F. M. Peeters, Phys. Rev. B **74**, 075404 (2006).
[14] S. Latil and L. Henrard, Phys. Rev. Lett. **97**, 036803 (2006).
[15] F. Varchon *et al.*, Phys. Rev. Lett. **99**, 126805 (2007).
[16] J. Hass *et al.*, Phys. Rev. B **75**, 214109 (2007).
[17] W. A. de Heer *et al.*, Solid State Commun. **143**, 92 (2007).
[18] I. Forbeaux *et al.*, Appl. Surf. Sci. **162**, 406 (2000).
[19] J. Hass *et al.*, Appl. Phys. Lett. **89**, 143106 (2006).
[20] Y. Baskin and L. Meyer, Phys. Rev. **100**, 544 (1955).
[21] A. N. Kolmogorov and V. H. Crespi, Phys. Rev. B **71**, 235415 (2005).
[22] T. Seyller *et al.*, Surf. Sci. **600**, 3906 (2006).
[23] C. Faugeras *et al.*, Appl. Phys. Lett. **92**, 011914 (2008).
[24] J. Hutcheon, in *Modern Aspects of Graphite Technology*, edited by L. Blackman (Academic Press, London, 1970).
[25] G. D. Barrera, J. A. O. Bruno, T. H. K. Barron, and N. L. Allan, J. Phys. Condens. Matter **17**, R217 (2005).
[26] M. Weinert, E. Wimmer, and A. J. Freeman, Phys. Rev. B **26**, 4571 (1982).
[27] G. Kresse and J. Hafner, Phys. Rev. B **47**, 558 (1993).
[28] J. P. Perdew and W. Yue, Phys. Rev. B **33**, 8800 (1986).
[29] G. Kresse and J. Hafner, J. Phys. Condens. Matter **6**, 8245 (1994).
[30] A. Incze, A. Pasturel, and P. Peyla, Phys. Rev. B **66**, 172101 (2002); A. Incze, Ph.D. thesis, Grenoble, France, 2002.
[31] J. M. B. Lopes dos Santos, N. M. R. Peres, and A. H. Castro Neto, Phys. Rev. Lett. **99**, 256802 (2007).
[32] W. T. Pong and C. Durkan, J. Phys. D **38**, R329 (2005).